Carbon nanocones under compression: Buckling and post-buckling behaviors

K. M. Liew, J. X. Wei, and X. Q. He
Department of Building and Construction, City University of Hong Kong, Kowloon, Hong Kong SAR
(Received 15 December 2006; published 24 May 2007)

The mechanical behavior of single-walled carbon nanocones (SWCNCs) with 19.2° apex angles under compression was investigated in the study reported herein. The analysis was performed using molecular dynamics simulation. Two different loading directions, i.e., axial compression and in-plane compression, were applied to study their influence on the strain energy of CNCs. We derived empirical formulas for calculating the critical strains of CNCs with various top radii that were subjected to both axial and in-plane compression. The results of the simulation reveal that cones under in-plane compression show a higher energy level than those under axial compression. In the buckling and post-buckling stage, each shape change, accompanied by an abrupt release of energy in the energy-strain curve, was analyzed. The possible reasons for early plastic failure were examined, with the buckling behavior of CNCs with geometrical parameters (top radius, bottom radius, and height) involved. Our computed results show that for the fixed ratio of height/bottom radius, CNCs with smaller top radii tend to be stiffer.

DOI: 10.1103/PhysRevB.75.195435 PACS number(s): 61.46.Fg, 81.07.−b

I. INTRODUCTION

Since the discovery of fullerenes[1] and carbon nanotubes,[2] the research community has paid much attention to carbon nanostructures. Sequent reports have shown that carbon is a flexible material that can form a variety of structures, such as carbon onions,[3] carbon boxes,[4] nanocapsules,[5] and carbon nanocones (CNCs).[6–8] The first study of CNCs claimed that closed cones could be uniquely determined by measuring the five distinct opening angles of 19.2°, 38.9°, 60°, 86.6°, and 123.6°, although only 19.2° angles were observed in samples.[6] The following report confirmed the existence of all five apex angles.[7] Later studies found that through precise control of the synthetic conditions, the tailoring of the morphology of CNCs was possible. The newly synthesized open CNCs had similar structures to closed cones, except that the tips were cut off.[9–12] Terrones *et al.*[10] and Muradov *et al.*[13] believed that open cones had very flexible structures, which could explain the difference between the angles observed in their samples and those in closed cones. However, Ekşioğlu *et al.*[14] proved that the open cone approach cannot explain the different apex angle observed in the sample, and that open cones should have the same apex angles as closed cones. Nevertheless, similar to CNTs, CNCs can also be categorized as single[7,8] and multiwalled.[9–12,15,16]

Despite active research activities in this area, theoretical work has fallen behind experimental studies. Researchers are still struggling to establish universally accepted approaches for CNC structures and growth mechanisms. Klein[17] developed a formal "topo-combinatoric" procedure for treating CNCs. Compernolle *et al.*[18] determined accurate geometries of CNCs of different sizes with a triangle, square, or pentagon at the apex using a quantum chemical optimization method. Ekşioğlu *et al.*[14] carried out comprehensive studies on the structures of CNCs by employing molecular models and structural analyzes.

Nevertheless, investigations into the mechanical properties of CNCs are scarce. Wei *et al.*[19] used continuum elastic theory and molecular dynamic (MD) simulation to show that the Young's modulus of a single-shell CNC is $\cos^4\theta$ that of an equivalent single-walled CNT (SWCNT). It should be noted that the CNC was simulated by applying tensile strain up to 5%, which meant that no buckling occurred and the detailed strain energy curve was not given. Jordan *et al.*[20] studied the mechanical chiral inversion of closed CNCs with large apex angles by compressing the cone tip with a spherical indenter using MD. They showed that the CNC can have true chiral inversion without breaking the chemical bonds.

Our earlier work[21] verified the implementation of Brenner's second generation potential by comparing our result of (8,0) CNT to those of other reported works. Because little theoretical research has been devoted to the simulation of CNCs, the validation of our results by comparing them with those of others was unrealizable.

In the study reported herein, the compressive properties of CNCs were investigated by employing the MD technique using Brenner's "second generation" reactive empirical bond-order (REBO) potential.[22] Preliminary buckling behavior was investigated for a single-walled open cone with an apex angle of 19.2°. Using regression approaches, empirical formulas were obtained for the critical strains of CNCs under both axial and in-plane compression deformations by fitting the MD simulations. The morphological changes and the energy release are discussed in detail here.

II. COMPUTATION MODEL

The numerical simulation was carried out by classical molecular dynamics simulation. The short-range interaction force between atoms was second-generation reactive empirical bond-order (REBO) potential of Brenner, as follows:[22]

$$E_{ij}^{\mathrm{REBO}} = V_R(r_{ij}) - \overline{b_{ij}} V_A(r_{ij}), \tag{1}$$

where $V_R(r)$ and $V_A(r)$ are the repulsive and attractive pair terms, and $\overline{b_{ij}}$ is the reactive empirical bond order between atoms.

For the long-range interaction force, the van der Waals potential was applied[23]

$$E_{ij}^{\mathrm{vdw}} = \begin{cases} 0, & r_{ij} < r_s', \\ c_{3k}(r_{ij} - r_k)^3 + c_{2k}(r_{ij} - r_k)^2, & r_s' \leqslant r_{ij} < r_m', \\ E^{\mathrm{LJ}}(r_{ij}), & r_m' \leqslant r_{ij} < r_b', \end{cases} \quad (2)$$

where $c_{n,k}$ are cubic spline coefficients, $r_s'=0.2$ nm, $r_m'=0.32$ nm, $r_b'=1.0$ nm, and E^{LJ} is defined as the Lennard-Jones 12-6 potential,[24] which is computed as

$$E^{\mathrm{LJ}} = 4\xi\left[\left(\frac{\sigma_{ij}}{r}\right)^{12} - \left(\frac{\sigma_{ij}}{r}\right)^{6}\right]. \quad (3)$$

Therefore, the potential sum becomes

$$E = \sum_i \sum_{j>i} (E_{ij}^{\mathrm{REBO}} + E_{ij}^{\mathrm{vdw}}). \quad (4)$$

As proposed by Mao *et al.*,[25] the van der Waals potential should be turned on only if the short-distance potential becomes zero. Otherwise, the steep repulsive wall of Lennard-Jones 12-6 potential in the short range can form an artificial reaction barrier.

The analysis in this study was carried out without temperature control. The equations of motion were investigated with Gear's predictor-corrector algorithm,[26] and the axial compression of open CNCs with 19.2° apex angles was achieved by applying an appropriate rate at one end and keeping the other end unmoved. At the beginning of each simulation, the CNC was allowed to equilibrate after being generated from two-dimensional (2D) graphene. The following stage involved recording the trajectories of the atoms, energies, and forces for later analysis. At this stage, the end atoms on one side were moved inwardly by small steps in two directions—axial or in-plane of the side surface as shown in Fig. 4, which is parallel to the initial CNC side surface with constant direction—whereas the other end of the nanocone remained unmoved. The inner atoms were relaxed and adjusted by the conjugate gradient minimization method. The atoms at both sides were not affected by the interatomic forces. Different from CNTs, the sides of CNCs are not parallel to the central axis. This significantly different configuration requires a very small loading rate for relaxation under compression. The smaller rate also demands more computational effort. In this study, we used 10 m/s as the applied rate on one end.

Among the five basic angles, the apex angle of 19.2° as observed in samples[7,8,13] is the smallest. In our simulation, all CNCs had apex angles of 19.2°. To avoid chiral inversion[20] and facilitate the application of strain rates, we studied open CNCs instead of their closed counterparts. The smallest upper diameter of our computed cases was 10 Å, which is in accordance with the theoretical prediction of the top radius of a CNC.[7] The structures of the computation cases were initially generated by folding over the graphene sheet with an overlap angle of 300°, as shown in Fig. 1; this is technically referred to as the disclination angle. This process produces closed CNCs, and the open CNC model can be established by cutting off the tip, as shown in Figs. 2 and 3.

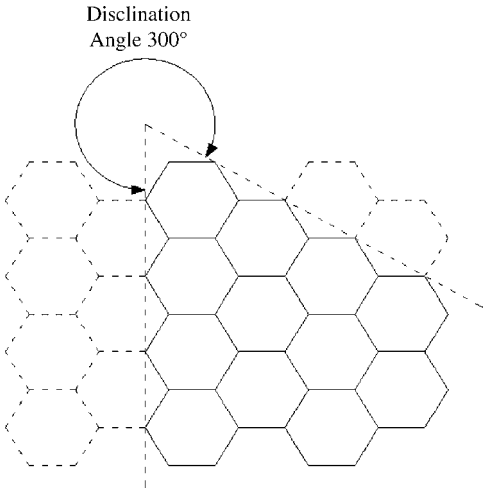

FIG. 1. Carbon graphene removed wedge with a disclination angle of 300°, ready to form the CNC.

III. NUMERICAL RESULTS AND DISCUSSION

A. A slender CNC ($H:R_b=4:1$)

To study the classic buckling behavior of CNCs under compression, a relative slender CNC was selected with the following parameters: $R_t=6$ Å, $R_b=18.5$ Å, $H=74$ Å. Each time step used in this simulation equals 1 fs, and the simulation lasts for 40 000 time steps. The applied compressions are along axial or parallel to side surface, respectively. The strain energy of the selected slender CNC (having 2211 atoms) versus strain are shown in Fig. 4. In the case of axial loading, as shown in Fig. 4, at small strain ($\varepsilon<0.034$) the CNC undergoes elastic deformation, and the total strain energy follows $E=0.5E''\varepsilon^2$. As the strain increases to $\varepsilon_a=0.0345$, which is associated with point a in Fig. 4, buckling occurs and the strain energy per atom drops significantly. The cone passes the linear elastic stage and enters the post-

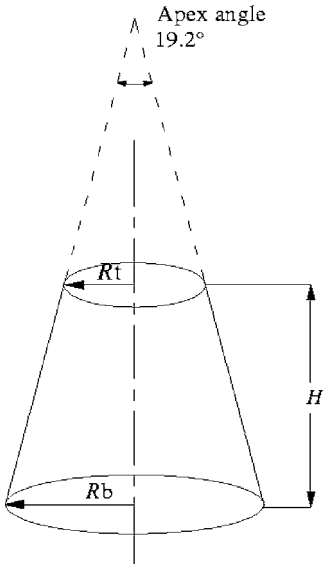

FIG. 2. Schematic illustration of the geometric parameters of the CNCs used in the study.

FIG. 3. (Color online) Schematic illustration of CNCs with R_t =10 Å, R_b=15 Å, and H=30 Å.

buckling stage. When the strain reaches ε_b=0.035, the energy has already decreased by 17.9% at critical point *b*, as shown in Fig. 4. The energy curves in the stage show approximate linearity by parts. At point *c* in Fig. 4, the strain is ε_c=0.037, with the energy increasing slightly by 1.75%. After a gap near point *d*, where ε_d=0.0377, the energy decreases by approximately 5.6%. As buckling develops, the curve climbs up again, which means that the increase of energy from compression cannot be totally eliminated by further energy dissipation from morphological changes, and energy starts to concentrate within the CNC again.

Figure 5 depicts the acute morphological changes as the deformation increases. When the compression is applied axially, the CNC starts to buckle at ε_a=0.0345, as shown in Fig. 5(a), being slightly concave in the vicinity of the top edge. The occurrence of local buckling leads to the loss of most symmetries of the CNC, leaving only one mirror plane through the *x*-*z* plane. The local buckling develops spontaneously until the other side becomes concave, as shown in Fig. 5(b), and eventually induces the plastic failure that accompanies the net release of strain energy. Further strain enhances this pattern until the kink forms a "fin" at point *c*, as shown in Fig. 5(c), followed by another energy release. As the fin develops (d), the configuration reorganizes itself and becomes two concave areas approximately perpendicular to the fin at ε_d=0.038, as shown in Fig. 5(d). The planes of symmetries increase to two, which are perpendicular to each other and cross the central axis. After the strain exceeds 0.038, the fin moves downward while the cone maintains the symmetries, and the strain energy starts to rise as shown in Fig. 5(e). In the case of in-plane compression, the geometrical shapes are similar to those in axial compression, except at point *C*, where the morphological changes are not as obvious but show a close resemblance to point *B*. The strain energy of each critical point for the axial loading is much smaller than that for in-plane compression.

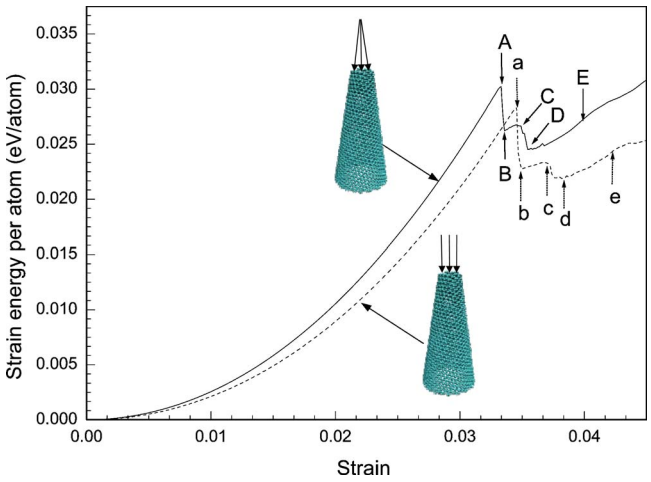

FIG. 4. (Color online) The dynamic response of the selected CNC with the ratio of the height to bottom radius H:R_b=4:1 under axial compression and in-plane compression, respectively.

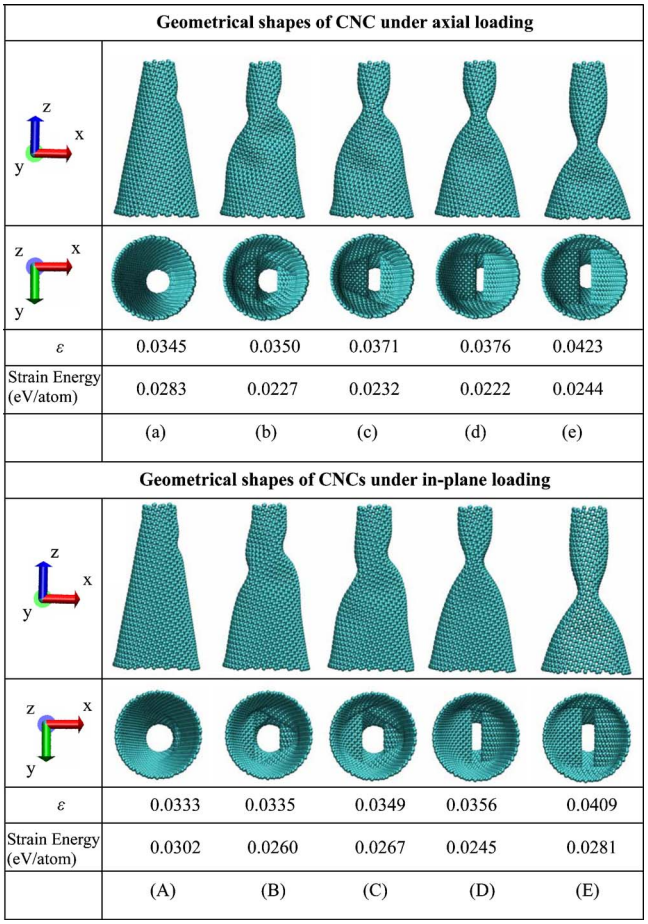

FIG. 5. (Color online) Morphological changes for the slender CNC (H:R_b=4:1) under in-plane loading and axial loading. The values underneath illustrate the strains and strain energies that correspond to each configuration.

Under axial compression, we compare the critical strain of CNC to that of a (10,10) CNT with the ratio of length/radius=6 in our previous report.[21] The radius in the middle of cone is 12.25 Å, giving that the ratio of length to middle radius equals 6, thus CNT and CNC have the same length/radius ratio and are comparable. The critical strain of the CNC for the buckling is 0.035 while the critical strain of the CNT is 0.067, implying a earlier post-buckling stage of

CNCs than CNTs when the ratio of length to radius of CNTs is equal to the ratio of length to middle radius of CNCs.

Local buckling occurs first near the edge as shown in Fig. 5(a) or, alternatively, the earlier buckling to the CNC can be attributed to the asymmetrical geometry about the middle plane or the inherent properties of the atomic carbon structures. If the former factor contributes to the early failure, then a different loading direction parallel to the side surface of the CNC should enhance the stiffness. To verify this hypothesis, the selected cone should be compressed using another loading direction, which is elaborated as follows.

The different response to applying the in-plane compression along the side surface of the CNC is shown in Figs. 4 and 5. The curve that represents in-plane compression demonstrates similar behavior to that which represents axial compression. The critical strain (point *A*) is 3.5% smaller than that in the case of axial loading; however, the energy level is 6.2% higher than the latter case. The energy spontaneously declines by 13.9% when it reaches point *B*. After that, a slight increase in energy occurs at point *C*, followed by a second drop at point *D*, reducing the energy by 8.24%. The curve then rises as the deformation propagates. The CNC shows a significant increase in stiffness when it is loading superficially rather than axially, which falls into our expectation as previously mentioned. The loading direction has a significant effect on the strain energy levels.

The geometrical details of the critical points under in-plane loading are provided in Fig. 5. The shapes generally agree well with those under axial loading, except point *C*. This can be interpreted as the in-plane compression rate having a very small horizontal component due to the sharp apex angle, but quite a large vertical component, which almost achieves the same value of axial loading. After buckling takes place, the CNC is less affected by the horizontal component than the vertical component, and tends to follow the buckling patterns that occur under axial compression. However, as shown in Fig. 5, the in-plane simulation returns even lower critical strain but higher critical energy. That can be explained in terms of force. The in-plane force can be decomposed into vertical and horizontal components. The axial force acted on the CNC under axial compression is larger than the vertical component of in-plane force acted on the CNC under in-plane compression, and thus the axial simulation gives greater strain than in-plane simulation. On the other hand, the axial force is smaller than the in-plane force (the resultant force of the vertical and horizontal components) which leads to a larger critical energy of the in-plane simulation.

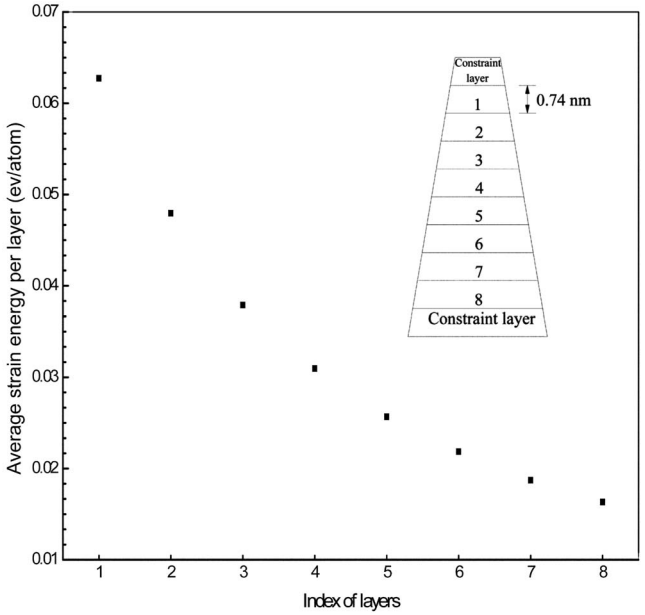

FIG. 6. Average strain energy per layer at critical strain. The cone is divided into 8 layers from top to bottom excluding the boundary layers at the endings. Height of each layer is 0.74 nm.

To show the energy distribution along the height of the CNC, the average energy per layer is introduced. Here, the average energy per layer is obtained from dividing the total energy of a layer by the number of atoms of the layer. Under axial compression, the distribution of the average energy per layer along the height of the cone is shown in Fig. 6 at the critical strain. It is observed that the average energy per atom is the highest at the top and decreases till the lowest at the bottom. This phenomenon is expected due to the fact that the strain decreases from the top layer to the bottom layer.

B. The effect of the top radius on the buckling of CNCs

To study the effect of the top radius on the buckling of CNCs, the height to bottom radius ratio was fixed as 2:1, and the critical strains of CNCs with various top radius from 10 Å to 25 Å were simulated. The results are given in Table I. The critical strain decreases as the top radius increases. Furthermore, the strain energy per atom of CNCs with vari-

TABLE I. Strain and energy at critical points of cones with different R_t for $H:R_b=2:1$.

				Critical point for axial loading		Critical point for in-plane loading	
R_t (Å)	R_{b-} (Å)	H_- (Å)	Atoms	ε_{cr}	Strain energy (eV/atom)	ε_{cr}	Strain energy (eV/atom)
10	15.11	30.22	928	0.0322	0.030	0.0311	0.031
15	22.66	45.32	2086	0.0241	0.015	0.0230	0.015
20	30.21	60.42	3699	0.0194	0.008	0.0189	0.008
25	37.77	75.54	5784	0.0170	0.006	0.0164	0.006

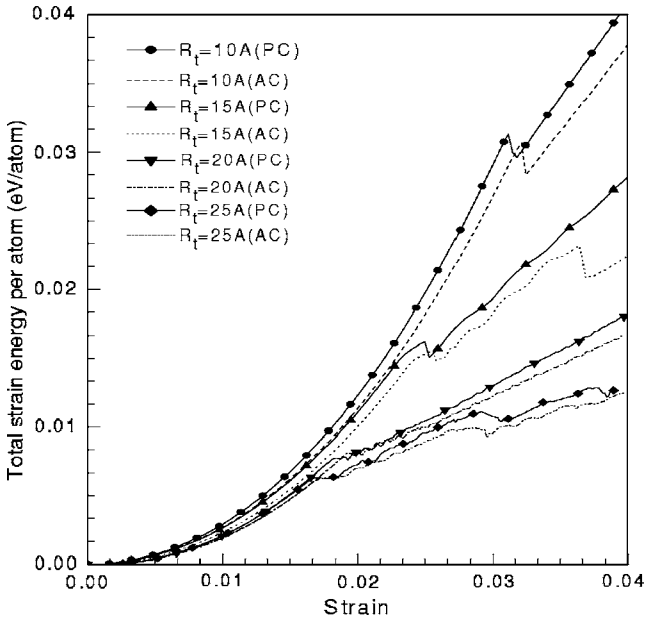

FIG. 7. Dependence of strain energy on the strain for open CNCs with the same H/R_b ratio but different top radii of 10 Å, 15 Å, 20 Å, and 25 Å, where PC stands for the in-plane compressive deformation, and AC represents axial compressive deformation.

ous top radii was simulated, and the results for axial compression and in-plane compression are displayed in Fig. 7. The curves show that under axial loading, the CNC with a smaller diameter has a larger critical strain and higher energy for the fixed height/bottom radius ratio. The strain energy of the cone with the smallest top diameter decreases by 5.4% after the buckling occurs, whereas the other cones show flat transitions from the elastic region to the plastic region rather than an obvious drop around the critical strain. The post-buckling behavior of R_t=10 Å predicts an approximately linear relationship between energy and strain. However, the other cones show very irregular behavior in the post-buckling region. In addition, in the case of in-plane loading, most parts of the energy curves in Fig. 7 are located above those in the axial loading, which means that there is an enhancement in the stiffness due to an alternative loading direction. The curves also tend to behave like those under axial loading. Nevertheless, differences of strains and energies at the critical points between the two loading directions are insignificant. Especially in the elastic region, the curves that stand for different loading directions are even closer for CNCs with larger upper diameters.

The critical strains of open CNCs with various top radii are plotted in Fig. 8 for the same ratio of H/R_b. Using regression analysis, two functions in the form of second order exponential decay were formulated to demonstrate the trends of critical strain as top radius R_t increases. Figure 8 shows that the critical strain drops quickly when the top radius is smaller. For a larger top radius, the critical strain decreases slowly with the increase of the top radius, thus indicating that the critical strain approaches a constant when the top radius is large enough. The two fitted curves are quite close to each other, showing a limited influence on the critical strain using different compression methods.

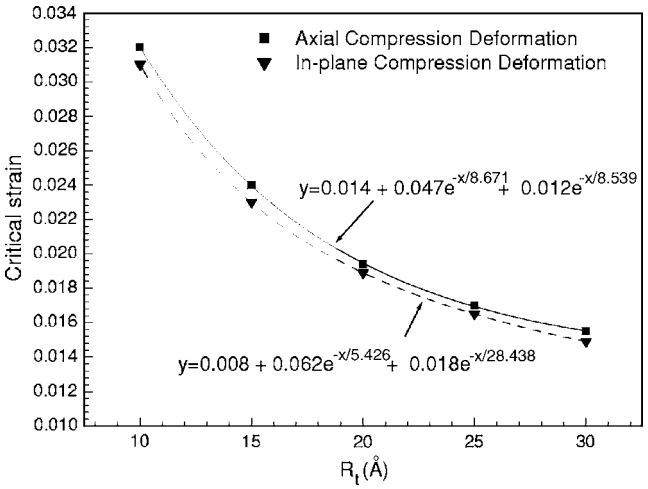

FIG. 8. Critical strain as a function of top radius for the open CNCs with the same H/R_b ratio.

C. The effect of height on the buckling of CNCs

To demonstrate the effects of different heights on the critical strain, the energy-strain curves of CNCs with the same top radius but different heights were calculated, and the results are shown in Fig. 9 and Table II for the case of axial compression. As illustrated in Fig. 4 and Fig. 7, the strain energies of CNTs under axial compression and under in-plane compression are very close; hence, the conclusion for CNCs under axial compression can also be applied to CNCs under in-plane compression. Figure 9 shows that as the height increases, the critical strain obviously decreases with the energy suddenly dropping from 11.49% to 26.45% for various heights, as shown in Table II. This occurs because

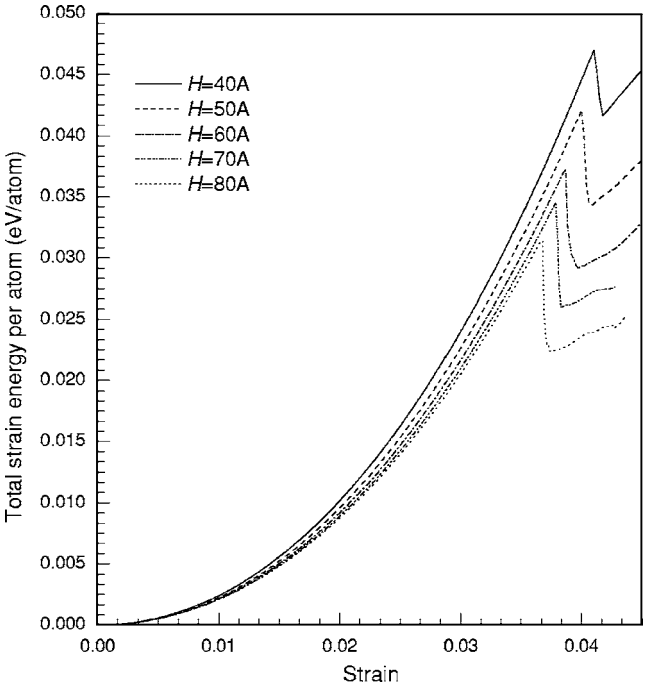

FIG. 9. Dependence of strain energy on the strain for the CNCs with the same top radius but different heights under axial loading.

TABLE II. Strain and energy at critical points of CNCs with same R_t but different H.

R_t (Å)	R_b (Å)	H (Å)	Atoms	ε_{cr}	Strain energy at critical point (eV/atom)	Energy drop percentage around critical points
5	12.08	40	821	0.041	0.047	11.49%
5	13.85	50	1124	0.04	0.042	17.86%
5	15.62	60	1475	0.039	0.037	19.19%
5	17.39	70	1864	0.038	0.035	25.71%
5	19.16	80	2294	0.037	0.031	26.45%

the higher the cone is, the greater its instability. The critical strain also shows the same tendency as the overall height increases, as shown in Table II. When the height of a cone increases from 40 Å to 80 Å, the strain decreases 0.001 per step in perfect unison. For different computation cases, the energy drops around the critical point are related to the cone height. The highest cone tends to present the largest energy drop percentage, which results from the large absolute energy drop as the numerator and the relatively small strain energy as the denominator, as shown in Fig. 9.

IV. CONCLUSIONS

In the study reported herein, single-walled open CNCs of different geometric configurations were investigated using the MD technique. Simple empirical formulas were obtained for the calculation of the critical strains of CNCs with various top radii under both axial compression deformation and in-plane compression deformation. Our computed results show that the critical strain and energy of CNCs are much smaller than those of their CNT counterparts. Their behavior beyond the elastic region shows no signs of brittleness or plasticity. The loading directions also have effects on buckling behavior and strain energy. In-plane compression induces larger strain energy than axial compression. In the case of a fixed ratio of height/bottom radius, the stiffness of a CNC with a smaller radius is greater than that of a CNT with a larger radius. The energy drop percentage around the critical point is related to height of the cone. Higher CNCs tend to lose more energy during the transition from the elastic region to the plastic region.

[1] H. W. Kroto, J. R. Heath, S. C. O'Brien, R. F. Curl, and R. E. Smalley, Nature (London) **318**, 162 (1985).
[2] S. Iijima, Nature (London) **354**, 56 (1991).
[3] D. Ugarte, Nature (London) **359**, 707 (1992).
[4] Y. Saito, and T. Matsumoto, Nature (London) **392**, 237 (1998).
[5] Y. Saito, K. Nishikubo, K. Kawabata, and T. Matsumoto, J. Appl. Phys. **80**, 3062 (1996).
[6] M. Ge and K. Sattler, Chem. Phys. Lett. **220**, 192 (1994).
[7] A. Krishnan, E. Dujardin, M. M. J. Treacy, J. Hugdahl, S. Lynum, and T. W. Ebbesen, Nature (London) **388**, 451 (1997).
[8] S. Iijima, M. Yudasaka, R. Yamada, S. Bandow, K. Suenaga, F. Kokai, and K. Takahashi, Chem. Phys. Lett. **309**, 165 (1999).
[9] N. A. Kiselev, J. Sloan, D. N. Zakharov, E. F. Kukovitskii, J. L. Hutchison, J. Hammer, and A. S. Kotosonov, Carbon **36**, 1149 (1998).
[10] H. Terrones, T. Hayashi, M. Muñoz-Navia, M. Terrones, Y. A. Kim, N. Grobert, R. Kamalakaran, J. Dorantes-Davila, R. Escudero, M. S. Dresselhaus, and M. Endo, Chem. Phys. Lett. **343**, 241 (2001).
[11] M. Endo, Y. A. Kim, T. Hayashi, Y. Fukai, K. Oshida, M. Terrones, T. Yanagisawa, S. Higaki, and M. S. Dresselhaus, Appl. Phys. Lett. **80**, 1267 (2002).
[12] M. Endo, Y. A. Kim, T. Hayashi, T. Yanagisawa, H. Muramatsu, M. Ezaka, H. Terrones, M. Terrones, and M. S. Dresselhaus, Carbon **41**, 1941 (2003).
[13] N. Muradov and A. Schwitter, Nano Lett. **2**, 673 (2002).
[14] B. Ekşioğlu and A. Nadarajah, Carbon **44**, 360 (2006).
[15] Y. Gogotsi, S. Dimovski, and J. A. Libera, Carbon **40**, 2263 (2002).
[16] G. Zhang, X. Jiang, and E. Wang, Science **300**, 472 (2003).
[17] D. J. Klein, Phys. Chem. Chem. Phys. **4**, 2099 (2002).
[18] S. Compernolle, B. Kiran, L. F. Chibotaru, M. T. Nguyen, and A. Ceulemans, J. Chem. Phys. **121**, 2326 (2004).
[19] C. Wei and D. Srivastava, Appl. Phys. Lett. **85**, 2208 (2004).
[20] S. P. Jordan, and V. H. Crespi, Phys. Rev. Lett. **93**, 255504 (2004).
[21] K. M. Liew, C. H. Wong, X. Q. He, M. J. Tan, and S. A. Meguid, Phys. Rev. B **69**, 115429 (2004).
[22] D. W. Brenner, O. A. Shenderova, J. A. Harrison, S. J. Stuart, B. Ni, and S. B. Sinnott, J. Phys.: Condens. Matter **14**, 783 (2002).
[23] S. B. Sinnott, O. A. Shenderova, C. T. White, and D. W. Brenner, Carbon **36**, 1 (1998).
[24] L. E. Lennard-Jones, Proc. R. Soc. London, Ser. A **106**, 441 (1924); **106**, 463 (1924).
[25] Z. Mao, A. Garg, and S. B. Sinnott, Nanotechnology **10**, 273 (1999).
[26] C. W. Gear, *Numerical initial value problems in ordinary differential equations* (Prentice Hall, New Jersey, 1971) Chapter 9.